Journal of Materials Processing Tech. 333 (2024) 118586

Contents lists available at ScienceDirect

Journal of Materials Processing Tech.

journal homepage: www.elsevier.com/locate/jmatprotec

Research Article

Surface morphology formation and subsurface microstructure evolution of zirconia in ultrasonic vibration-assisted burnishing

Weihai Huang, Toshiki Tsuchida, Jiwang Yan *

Department of Mechanical Engineering, Faculty of Science and Technology, Keio University, Hiyoshi 3-14-1, Kohoku-ku, Yokohama 223-8522, Japan.

ARTICLE INFO

Keywords:
Burnishing
Ultrasonic vibration
Microstructure evolution
Surface integrity
Yttria stabilized zirconia

ABSTRACT

Yttria-stabilized zirconia (YSZ) is an outstanding ceramic material with applications in dentistry, biomedical, and mechanical device, where a smooth and durable surface is required. This study employed ultrasonic vibration-assisted burnishing (UVB) to enhance the surface hardness of YSZ while simultaneously reducing its roughness. The surface topography formation, subsurface microstructure evolution, and surface hardness change of YSZ were investigated. It was found that a smooth surface with an average roughness (Ra) of 0.12 μm was achieved using UVB, representing 67.6 % reduction in surface roughness from the original sintered surface, which is attributed to the burnishing-to-cutting phenomenon during the processing. The UVB-induced compression and material densification prevented the formation of the monoclinic phase during the processing of YSZ. Grain refinement and crystal lattice distortion occurring in the subsurface layer led to an increase in surface hardness, reaching up to 19.7 % higher than that of the original sintered surface. Moreover, the UVB-processed surface demonstrated a high resistance to mechanical impacts, effectively inhibiting the tetragonal-to-monoclinic phase transformation in indentation testing. These findings demonstrate that UVB is an effective approach for enhancing the surface and subsurface properties of the material.

1. Introduction

Yttria stabilized zirconia (YSZ) ceramic, with excellent mechanical properties and biocompatibility, is widely used in dental implants [1] and load-bearing components [2], serving as a potential alternative to traditional metals. Due to yttria doping, YSZ is primarily composed of a stable tetragonal phase with a small amount of monoclinic phase, resulting in relatively high strength and fracture toughness compared to pure zirconia, which is predominantly composed of the monoclinic phase [3,4]. This is because under external mechanical load, the tetragonal phase would change to the monoclinic phase, accompanied by volume expansion. Consequently, although microcracks tend to occur in the material, the volume expansion results in compressive stress at the crack tip, which inhibits crack propagation [5]. Nevertheless, similar to other ceramics, YSZ is hard and brittle; therefore, its surface finishing is usually achieved through polishing [6], grinding [7], and nano-cutting [8]. Moreover, to further enhance the machinability of YSZ, grinding [9] and cutting [10] assisted by laser irradiation, as well as tool heating [11], have also been attempted. However, these methods may reduce the surface's ability to resist external mechanical loads in service, either due to mechanical machining-induced tetragonal-to-monoclinic (t-m) phase transformation [12,13] or thermal damage [14,15]. For this reason, alternative surface processing technologies are needed to smoothen the surface, and at the same time, harden the surface layer to enhance its ability of withstanding external loads and contact damages.

Burnishing is a surface finishing technique where a ball tool slides across the workpiece surface, inducing plastic deformation in the work material [16,17]. Additionally, it is effective for surface modification, enhancing wear resistance, fatigue limit, and inducing residual compressive stress in the work material [18], while also reducing surface porosity [19]. Burnishing has found widespread application in processing ductile metals, including various alloys [20,21] and stainless steels [22]. To enhance the performance of burnishing, ultrasonic vibrations have also been introduced to the tool, with the direction of vibration perpendicular to the workpiece surface [23,24], which is known as ultrasonic vibration-assisted burnishing (UVB). This was done to allow the tool to strike the material, creating a hammering effect perpendicular to the workpiece surface and minimizing resistance in the burnishing direction.

While extensive research has been conducted on the burnishing of

* Corresponding author.
E-mail address: yan@mech.keio.ac.jp (J. Yan).

https://doi.org/10.1016/j.jmatprotec.2024.118586
Received 20 June 2024; Received in revised form 1 September 2024; Accepted 4 September 2024
Available online 5 September 2024

ductile metals, studies on brittle materials are relatively few, as inducing plastic deformation of brittle materials without causing crack formation presents a significant challenge. A recent attempt has been made to utilize micro/nano burnishing for processing zinc selenide crystals, demonstrating that brittle materials can be burnished without forming cracks [25]. The burnished surface exhibits lower roughness compared to the original surface, and strain hardening of the material has been observed. Although, plastic deformation induced the appearance of dislocations and lattice distortions in the shallow subsurface induced by plastic deformation, no phase transformation has occurred in the burnished surface. Following this, a feasibility study on UVB of YSZ was conducted, utilizing a flexible workpiece stage and a rotating tool to enable shape-adaptive surface conditioning [26]. The surface roughness was successfully reduced through UVB. However, as the study mainly focused on the development of processing techniques for YSZ, the differences in processing characteristics from those of metal burnishing, and the mechanisms behind the surface morphology formation of YSZ remain unclear. Moreover, unlike the burnishing of zinc selenide crystals, phase transformations related to processing conditions have been observed in the burnished surface of YSZ [26]. Given that the microstructure constituents in YSZ significantly affects its performance under mechanical load, understanding the mechanisms of phase transformation during burnishing process is essential for microstructure modulation. However, to date, the subsurface microstructure evolution of YSZ under burnishing has not been clarified, and whether this subsurface microstructural change induces a surface hardening effect has not yet been experimentally validated.

In this study, UVB experiments were conducted on YSZ under various conditions and compared with those results obtained through conventional burnishing (CB). The surface formation mechanism in YSZ burnishing was investigated by examining the morphology and roughness of the workpiece surface, as well as characterizing the tool surface before and after burnishing. The subsurface microstructure evolution under UVB was investigated using cross-sectional transmission electron microscopy observations and micro-Raman spectroscopy analyses. Their mechanisms were illustrated and compared with those of CB, cutting, and indentation. The effect of ultrasonic vibration on the burnishing performance was identified. Finally, the UVB-induced surface hardening effect was validated by nanoindentation tests, and the resulting subsurface damages were characterized. The results of this study are anticipated to advance the future manufacturing of YSZ parts, enhancing their surface functionality. They also serve as a reference for processing other advanced ceramics, thereby improving their integrity and functionality.

2. Material and methods

Fully sintered YSZ with 3 mol% Y_2O_3, which has a grain size of ~500 nm was used as the workpiece. The workpiece dimensions are 9.7 × 10.6 × 2.7 mm. The hardness, fracture toughness, and Young's modulus are 12.5 GPa, 6.0 MPa $m^{1/2}$, and 210 GPa, respectively. The workpiece has a sintered surface finish without any preprocessing, with a surface roughness of ~0.37 μm Ra.

Burnishing experiments were conducted on an X-Y-Z axis machine tool equipped with an ultrasonic vibration unit (AREUSE Ltd., Japan) on the Z-axis, as shown in Fig. 1a. The workpiece was fixed in a tank filled with oil for lubrication. Fig. 1b shows a schematic of the UVB process, during which the tool slides on the workpiece surface along *y*-direction, meanwhile the tool vibrates in *z*-direction. The vibration frequency of the tool was 27 kHz, and the amplitude was 2 μm. Different forces of 50 N, 100 N, and 200 N were applied normal to the workpiece surface for the burnishing process, which was monitored by a piezoelectric dynamometer (9256C2, Kistler Co. Ltd., Switzerland). The corresponding burnishing depths were approximately 3.3 μm, 5.2 μm, and 6.5 μm, respectively. Various burnishing speeds and numbers of burnishing cycles were also applied during the processing. To ensure a consistent burnishing speed across all contact areas, the tool rotation function was not used. CB experiments were performed under the same processing parameters as the UVB ones for comparison. The detailed processing parameters for each experiment are listed in Table 1.

A burnishing tool made of polycrystalline diamond, having a hemispherical tip of 1.5 mm radius, was used for burnishing, as shown in Fig. 2a. A microscope image and a topographic map of the tool's top surface are presented in Fig. 2b and c, respectively. SEM images of the tool surface at low and high magnifications are shown in Fig. 2d and e, respectively, for comparison with the surface of the tool after it has been used. Many irregular protrusions in the range of several hundred nanometers to several micrometers were observed on the tool surface. A typical surface profile of the tool, extracted along line A–A' indicated in Fig. 2c, is plotted in Fig. 2f. The average roughness (Ra) and maximum profile valley depth (Rv) of the tool surface were 1.3 μm and 5.3 μm, respectively.

Table 1
Processing parameters of burnishing experiments.

Parameters	Values
Burnishing force (*F*)	50, 100, 200 N
Burnishing speed (v_c)	0.3, 3, 30, 60, 120 mm/s
Number of burnishing cycle (*N*)	1, 10, 20, 30
Vibration frequency (*f*)	0 (CB), 27 kHz (UVB)
Vibration amplitude (*A*)	0 (CB), 2 μm (UVB)

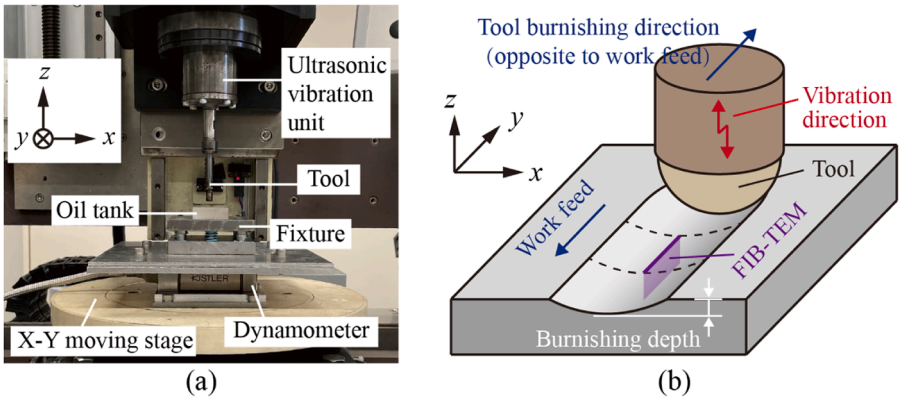

Fig. 1. Configuration of the burnishing experiments: (a) photograph of the experimental setup; (b) schematic of the ultrasonic vibration-assisted burnishing (UVB) process. After UVB processing, focused ion beam (FIB) milling was performed at the bottom of the burnished groove to create a lamella for transmission electron microscopy (TEM) observation.

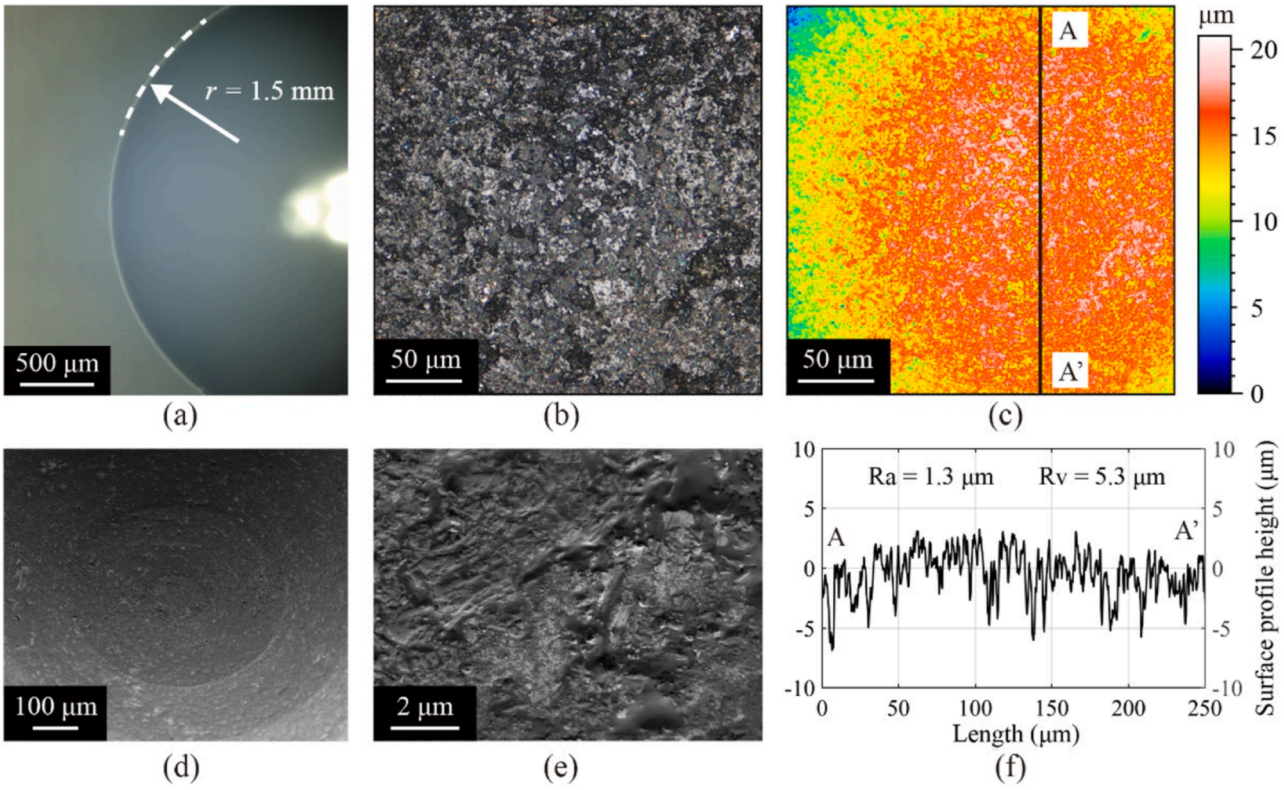

Fig. 2. Characterization of the unused burnishing tool: (a) a microscope image of the side view of the tool; (b) and (c) are a microscope image and a topographic map, respectively, of the tool surface at the same location on the tool tip; (d) and (e) are SEM images of the tool surface at low and high magnifications; and (f) a surface profile of the tool extracted along line A–A' indicated in (c).

After burnishing, the workpiece surfaces were observed by a scanning electron microscope (SEM) and measured by a white light interferometer. The crystalline phase of YSZ was analyzed by a laser micro-Raman spectrometer. Cross-sectional observation of the workpiece subsurface microstructure was conducted with a transmission electron microscopy (TEM). The TEM lamella was prepared by a focused ion beam (FIB) system. Prior to this, osmium oxide layer and carbon layer were coated on the workpiece for surface protection. The surface morphology of the burnishing tool was characterized by an SEM equipped with energy dispersive X-ray spectroscopy (EDX) detector.

Finally, a nanoindentation device (ENT1100a, Elionix Inc., Japan) equipped with a diamond Berkovich indenter was used to evaluate the changes in surface mechanical properties after burnishing. The maximum applied load for nanoindentation tests was 50 mN and 1000 mN, respectively. The loading/unloading rate for the indentation tests was 1 mN/s.

3. Results and discussion

3.1. Surface morphology characterization

Fig. 3a shows an overall view of the original surface of the fully sintered YSZ. Several protrusions, each tens of microns in size, were visible, along with a multitude of submicron-scale particles dispersed across the entire surface. These planar irregularities result from the growth of crystal grains during YSZ sintering. From an enlarged view, as shown in Fig. 3b, ultrafine grains and their grain boundaries are clearly observable. CB- and UVB-processed surfaces were observed on the same scale as the original surface. In the overall view of the surfaces after CB and UVB (see Fig. 3c and e, respectively), the large protrusions and small particles disappeared; however, many fine marks characterized by white lines parallel to the burnishing direction were observed on the surfaces, compared to the original surface (see Fig. 3a). In particular, the fine marks on the CB-processed surface are more numerous and pronounced compared to those on the UVB-processed surface. By enlarging the CB-processed surface (see Fig. 3d), it is evident that the grain boundaries disappeared, and no cracks were formed. Additionally, the fine marks resemble burrs, which may be caused by extrusion during burnishing using a tool with a rough surface profile. In contrast, upon examining the UVB-processed surface at higher magnification (see Fig. 3f), the formation of burr-like marks was less significant. By analyzing with ImageJ software, the burr area formed by CB accounts for 10 % of the observed area in Fig. 3d, while the burr area formed by UVB is reduced to 2 % in Fig. 3f. This may be because vibrations enhance lubrication, thereby reducing the extent of extrusion. In addition, unlike the CB-processed surface, where all grain boundaries had disappeared, some blurred grain boundaries were left on the UVB-processed surface. The blurred boundaries indicate that the material within the area tended to deform through compression rather than being removed, similar to observations in indentation [27]. Since the blurred boundary area is a narrow strip oriented along the burnishing direction, it may be attributed to insufficient tool-workpiece contact, which is due to the combination of tool vibration and a rough tool surface. Increasing the burnishing cycles can effectively enhance the uniformity of the burnished YSZ surface.

A high-magnification image of the UVB-processed surface is shown in Fig. 4a. In addition to the burr-like marks, numerous periodic marks were imprinted on the burnished surface along the burnishing direction, which results from the hammering effect induced by tool vibration. However, these vibration marks appear randomly perpendicular to the burnishing direction and exhibit various shapes, as marked by the white lines in Fig. 4a. This phenomenon is also attributed to the rough tool surface, where certain irregular submicron-scale protrusions, as seen in Fig. 2e, impact the work material during tool vibrations. Fig. 4b displays a high-magnification image of the UVB-processed surface, focusing on

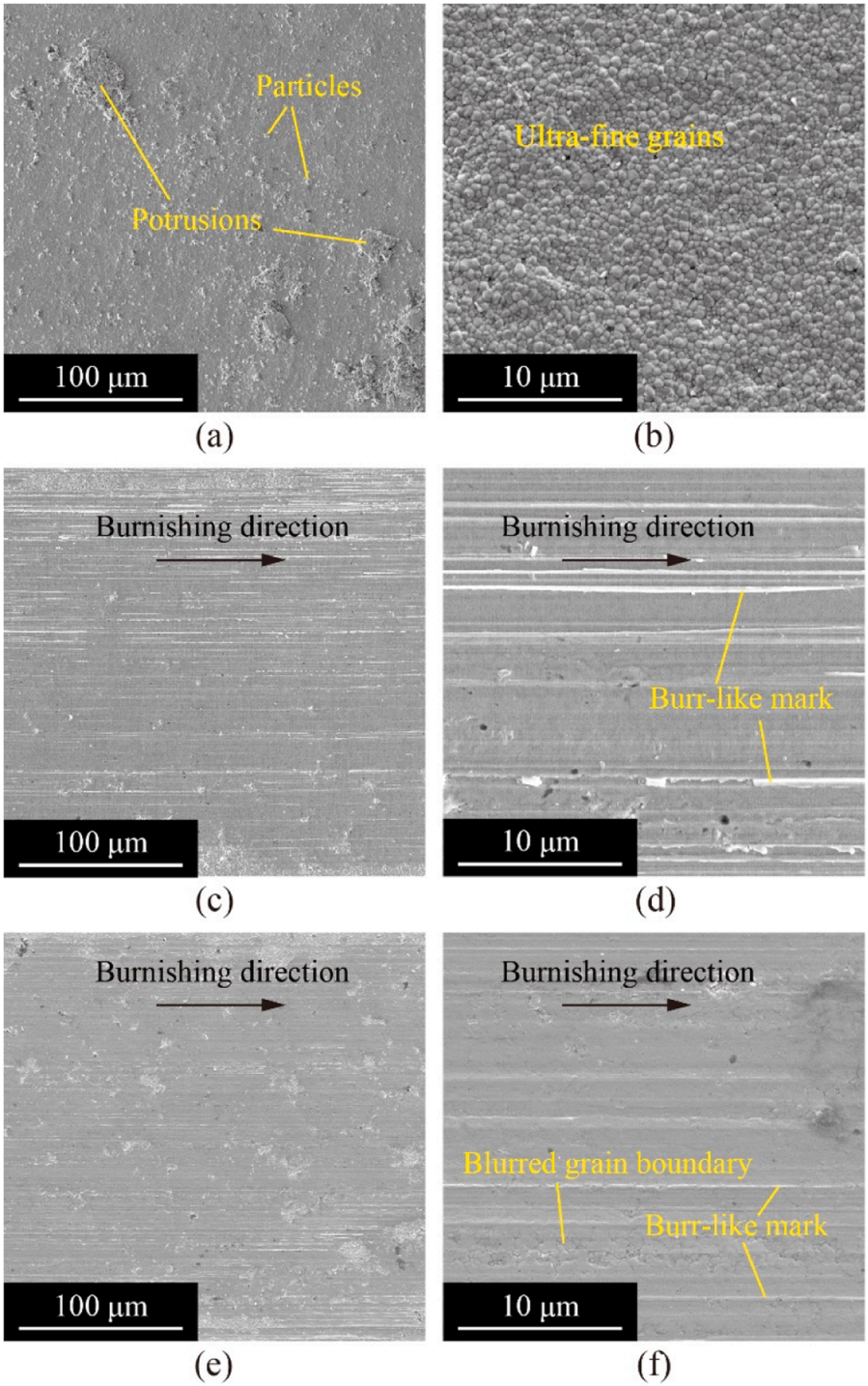

Fig. 3. SEM images of yttria-stabilized zirconia surfaces: (a) and (b) are the overall and enlarged views of the original surface; (c) and (d) show the surface after conventional burnishing; (e) and (f) show the surface after ultrasonic vibration-assisted burnishing. Each burnishing test was performed under a force of 100 N, speed of 3 mm/s, and for 1 cycle.

the boundary of the tool-work contact area. It is evident that crystal grains can be shaved off by the rough-surfaced tool during burnishing. Chips adhering to the processed surface were also observed. Thus, it can be inferred that during the burnishing of YSZ, at the microscopic level, certain local irregularities on the tool surface may act as abrasive grits, removing the work material in a ductile manner. Meanwhile, at the macroscopic level, the hemispherical tool plastically deforms the work material. A burnishing-to-cutting phenomenon has been observed in the burnishing of YSZ, which will discussed further in Section 4.1. This is somewhat akin to the reverse of the cutting-to-burnishing phenomenon observed in metal grinding [28].

3.2. Surface roughness analysis

To further analyze the deformation of YSZ caused by burnishing, the 3D topographies of the burnished surfaces were characterized. As an example, Fig. 5a displays the surface after 30 cycles of UVB processing. Two surface profiles perpendicular to the burnishing direction

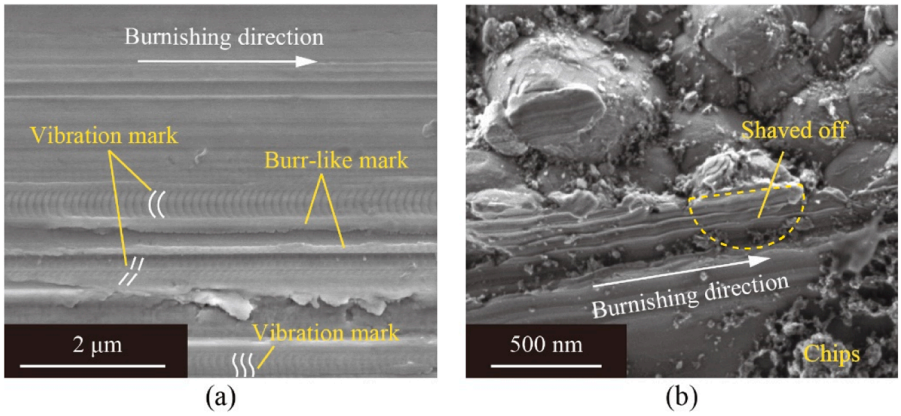

Fig. 4. High-magnification SEM images of the yttria-stabilized zirconia surfaces after ultrasonic vibration-assisted burnishing at different regions: (a) center of the tool-workpiece contact area, (b) boundary of the tool-workpiece contact area. The burnishing test was performed under a force of 100 N, speed of 3 mm/s, and for 1 cycle.

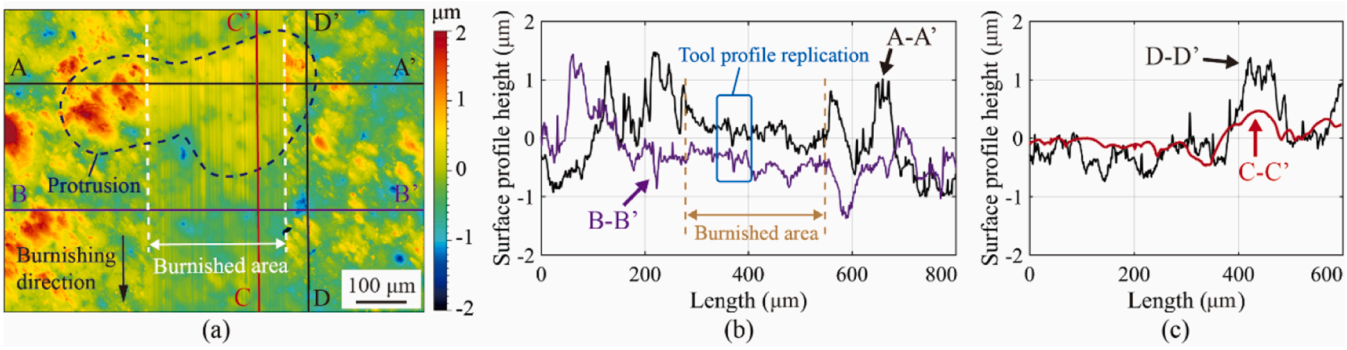

Fig. 5. Surface topography of yttria-stabilized zirconia after ultrasonic vibration-assisted burnishing: (a) white light interferometer topographic image; (b) surface profile perpendicular to the burnishing direction [along lines A–A' and B–B' indicated in (a)]. (c) surface profile parallel to the burnishing direction [along lines C–C' and D–D' indicated in (a)]. The burnishing test was performed under a force of 100 N, speed of 3 mm/s, and for 30 cycles.

(indicated by lines A–A' and B–B' in Fig. 5a) were extracted and plotted in Fig. 5b. Additionally, the surface profiles of the burnished and unburnished areas, parallel to the burnishing direction (indicated by lines C–C' and D–D' in Fig. 5a), were extracted and plotted in Fig. 5c. It is evident from Fig. 5a that the topography of the burnished area is more uniform than that of the original surface, especially in areas where protrusions were present. Moreover, it is worth noting that the areas where the protrusions originally existed remained higher than other areas after burnishing. This suggests that the burnishing process primarily induces local deformation rather than material removal, unlike the cutting process. From this perspective, the burnishing process is effective for smoothing the YSZ surface without altering the macroscale shape of the workpiece surface. In the direction perpendicular to the burnishing direction, Fig. 5b shows that the profiles in the burnished area exhibit small and dense fluctuations without sharp peaks, which is distinct from those in the unburnished area where there are large and sparse fluctuations. Besides, it can be observed that the two profiles exhibit the same shape within certain parts of the burnished area, indicating that the tool surface profiles could be effectively replicated onto the workpiece surface under complete tool-work contact conditions. In the burnishing direction, Fig. 5c clearly demonstrates that, before burnishing, the surface profile exhibits numerous sharp peaks and valleys. After burnishing, all the sharp features of the surface profile have become rounded. Nevertheless, the profiles in the burnished areas still contain some noticeable valleys, which hinders further reduction in the fluctuating value of the surface profiles. This is attributed to the high hardness of YSZ and its limited plastic flow compared to metals, which prevents the protruding material from being pushed into the surface cavities during the burnishing process [29].

Fig. 6 compares the average roughness (Ra) of YSZ surfaces burnished under various conditions. To avoid interference from the tool surface profile, roughness measurements were taken along the burnishing direction. It can be seen from Fig. 6a that, after burnishing with a force of 50 N, the roughness decreased from its original value of 0.37 μm Ra to approximately 0.22 μm Ra. When the force increased to 100 N, the surface roughness reached a minimum of 0.18 μm, representing a 51.4 % improvement from the original surface roughness. Upon further increasing the force to 200 N, however, the burnished surface became rougher compared to the conditions of 50 and 100 N; nevertheless, it remained smoother than the original surface. The phenomenon in which surface quality begins to deteriorate when the burnishing force exceeds a critical value is similar to that observed in the burnishing of metals [30]. This is because with a further increase in the burnishing force, the tool penetrates deeper into the work material; as a result, the tool tends to remove material by ploughing rather than plastically deforming it by compression [31]. It is also worth noting from Fig. 6a that under the same burnishing force, the UVB and CB produced similar surface roughness values, which differs from metal burnishing where UVB achieved a significantly better surface finish compared to CB [32]. This is supposed to be caused by the inherent properties of YSZ, which has ultrafine and hard grains. It has been known that grain boundaries are defects in the crystal structure [33], which disrupts the motion of dislocations through the material. The ultrafine grains, indicating a very high grain boundary density. Therefore, the dense grain boundaries intensively impede dislocation glide, limiting plastic flow and making it difficult for the protruding material to be pushed into the

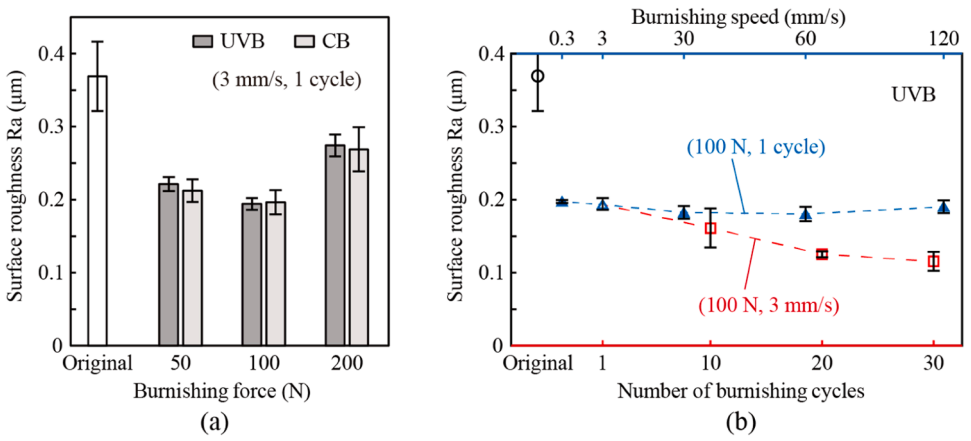

Fig. 6. Average roughness of the burnished surfaces: under various (a) burnishing forces, and (b) burnishing speeds and numbers of burnishing cycles. The blue dashed line and the red dashed line indicate the trends in surface roughness variation with burnishing speed and the number of burnishing cycles, respectively. UVB refers to ultrasonic vibration-assisted burnishing, while CB refers to conventional burnishing. The error bars represent the standard deviations from the mean values.

surface cavities, even with tool vibration.

Fig. 6b depicts the influence of the burnishing speed and number of cycles on the surface roughness. The change in burnishing speed had no significant effect on the surface roughness. Previous studies have reported that in the grinding of YSZ, surface roughness notably decreased until the processing speed increased to between 40 m/s and 80 m/s [34]. Therefore, during the burnishing of YSZ, where the fastest burnishing speed is 120 mm/s, such a slow processing speed is considered to result in negligible thermal effects, thereby having almost no impact on surface roughness. In contrast to the burnishing speed, a clear trend was observed where surface roughness decreased as the number of burnishing cycles increased. After 30 cycles, the smoothest surface was obtained exhibiting 0.12 μm Ra, indicating a 67.6 % reduction from the original surface roughness. This is thought to occur because during each burnishing cycle, the area of the workpiece contacted by the tool changes. As the tool moves repeatedly across the surface of the workpiece, it gradually forms a smooth surface by burnishing the areas that were either not contacted or insufficiently burnished during previous burnishing cycles.

3.3. Material phase analysis

Raman spectra were measured to detect phase transformations in burnished surfaces under different conditions. Fig. 7 plots these spectra and compares them with the spectrum of the original surface. All spectra exhibit similar features, with six main peaks located at 147, 264, 327, 472, 613, and 636 cm^{-1}, respectively, as marked in the graph, indicating that the work material was composed of monoclinic (m) and tetragonal (t) phases [35]. Furthermore, a weak monoclinic doublet at 180–190 cm^{-1} was observed on the original surface. In contrast, for the burnished surface, the shape of the monoclinic doublet exhibits some changes, indicating a possible phase transformation. To quantitatively analyze the change of tetragonal phase to monoclinic phase, the monoclinic volume fraction V_m was defined using formula [36]:

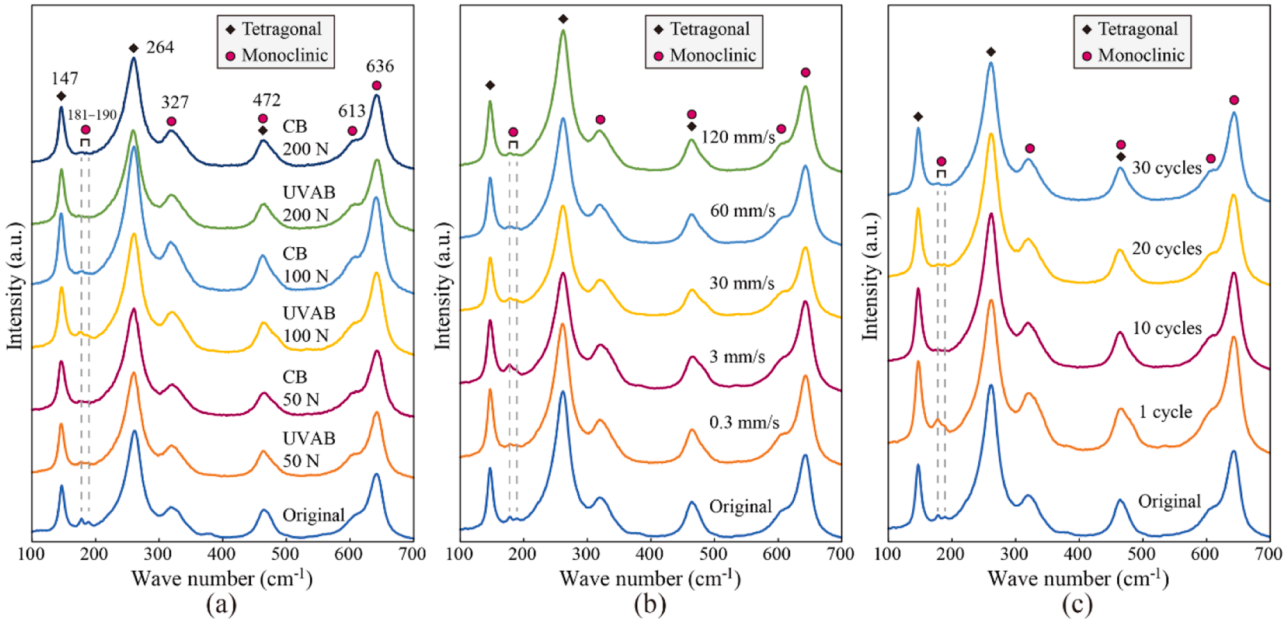

Fig. 7. Comparison of Raman spectra of the burnished surfaces: under (a) ultrasonic vibration-assisted burnishing (UVB) and conventional burnishing (CB) with various burnishing forces at a speed of 3 mm/s and for one cycle, (b) UVB with various burnishing speeds at a force of 100 N and for one cycle, and (c) UVB with various numbers of burnishing cycles at a force of 100 N and a speed of 3 mm/s.

$$V_m = \frac{I_m^{(181)} + I_m^{(190)}}{2.07 \times I_t^{(147)} + I_m^{(181)} + I_m^{(190)}} \quad (1)$$

where I indicates the integrated intensity of the peaks. The superscript numbers designate the Raman shift of peaks, with subscripts m and t indicating the monoclinic and tetragonal phases, respectively.

Fig. 8 plots the V_m of the surfaces burnished under various conditions. All burnished surfaces have a smaller V_m compared to the original surface. In other words, the burnishing process inhibited tetragonal phase from changing to monoclinic phase. The mechanism of this effect will be discussed in Section 4.2. Notably, in one-cycle burnishing, the V_m changed in an unstable manner (Fig. 8a,b). This instability could be attributed to the rough original surface and the hard property of the material, which caused poor contact with the tool during the initial cycle of burnishing. As the number of burnishing cycles increased, both the average value of V_m and its deviation were significantly reduced. The V_m remained stable as the number of burnishing cycles increased beyond 10 (Fig. 8c) due to the surface flattening effect. Additionally, the UVB-processed surface displays a higher V_m compared to CB when subjected to a larger burnishing force. This may be due to the tetragonal phase partially changing to a disordered phase under UVB, as suggested by TEM observations (discussed in the following subsection), which leads to a smaller denominator in Eq. (1).

3.4. Subsurface cross-sectional observation

The subsurface microstructure of the original workpiece, that is, the workpiece before the burnishing process, was first observed by cross-sectional TEM as a reference. A general view of the subsurface microstructure is shown in Fig. 9a. It can be seen that many grains with random shapes compose the bulk. The surface profile of the workpiece resembles a wave, with valleys primarily at the junctions of two grains. The close-up views of the subsurface regions located close to and far from the surface are shown in Fig. 9b and c, respectively. The sizes of the grains are on the same scale, and the grain boundaries can be clearly distinguished. The electron diffraction patterns within the near-surface and far-surface regions show spot patterns, indicating there is no significant stress or deformation in either the surface or the interior of the original workpiece.

A general view of the subsurface microstructure of the workpiece processed by UVB is shown in Fig. 10a. The profile of the surface became flat due to the processing, compared to Fig. 9a. Additionally, in the entire subsurface region, no cracks formed after burnishing, in contrast to the subsurface machined by grinding [15] and cutting [12] under large cutting forces, where cracks were formed. The close-up view of the subsurface regions located close to the surface is shown in Fig. 10b. The original individual grains and their boundaries became invisible. A layer of structural change with a thickness of approximately 90 nm formed just beneath the surface, which was characterized by some lines parallel to the surface plane. The electron diffraction pattern within this layer tended to form a ring-like pattern, as shown in the upper left of Fig. 10f. This implies that burnishing results in a densified layer with grain refinement in the near-surface region. In contrast, in the subsurface region located far from the surface, as shown in Fig. 10c, the grain boundaries remained clear as in the original workpiece. The diffraction pattern (see the upper right of Fig. 10f) displayed spot patterns, suggesting that the grains in this deep region remained free from deformation compared to the near-surface region. A magnified view of the densified layer is shown in Fig. 10d. Nanocrystals are clearly observed within this region. A high-magnification image of the nanocrystals is shown in Fig. 10e, which reveals that the nanocrystals have lattices oriented in various directions surrounded by disordered areas. This distinction can be observed in the fast Fourier transform (FFT) results shown in lower left and right of Fig. 10f, where the disordered areas and nanocrystals display halo rings and spot patterns, respectively. The lattice distance of the nanocrystal in Zone2 was calculated to be approximately 0.1232 nm, suggesting that the nanocrystal may have a tetragonal phase reflecting (104) or a monoclinic phase reflecting (330). The specific phase requires further identification.

Fig. 11a shows the subsurface microstructure of the workpiece processed using CB. Similar to the surface produced by UVB, no microcracks were observed in the entire subsurface region. The close-up view of the subsurface regions located close to the surface is shown in Fig. 11b. Unlike UVB, which generated a continuous dense layer in the near-surface region, CB resulted in dispersed densified zones. The diffraction pattern within the near-surface region (see the upper left of Fig. 11f) suggests that the material underwent lattice distortion, though not as severe as in UVB. In other words, UVB produced a more severe plastic deformation than CB, resulting in a significantly denser layer. A discussion of this phenomenon is provided in Section 4.2. In the subsurface region located far from the surface, as shown in Fig. 11c, the grain features were similar to those in the original workpiece. The diffraction pattern in the upper right of Fig. 11f presented a spot pattern, implying that this region was less affected by the burnishing process. A magnified view of the near-surface layer is shown in Fig. 11d. Some nanocrystals were observed within the grains just beneath the burnished surface. A high-magnification image of the nanocrystals is presented in Fig. 11e. Two different spot patterns are observed in the FFT results of the two typical nanocrystals, as shown in the lower left and right of Fig. 11f, indicating that these nanocrystals have lattices oriented in different directions. The variation in lattice arrangement direction for the nanocrystals may be due to inherent defects within the grains, which could promote diverse dislocation nucleation. Fig. 11g presents the elemental mapping of a typical area containing a densified zone. The atomic percentage of elements was plotted along the white line based on the average within the area marked by the white dashed box. It can be seen

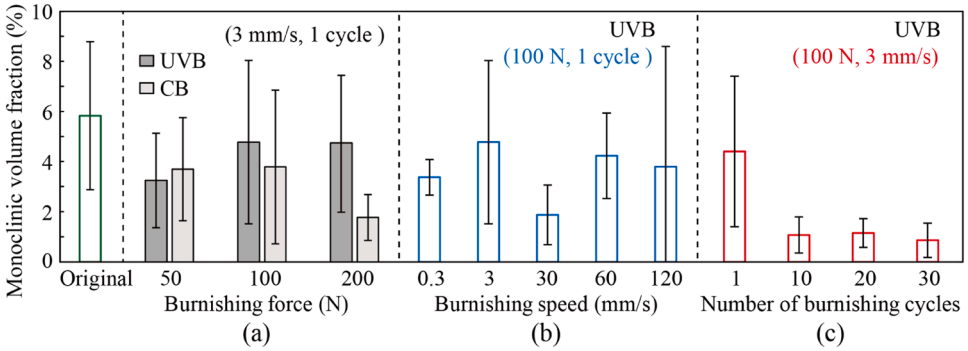

Fig. 8. Change in monoclinic volume fractions of the burnished surfaces: under various (a) burnishing forces, (b) burnishing speeds, and (c) number of burnishing cycles. UVB refers to ultrasonic vibration-assisted burnishing, while CB refers to conventional burnishing. The error bars represent the standard deviations from the mean values.

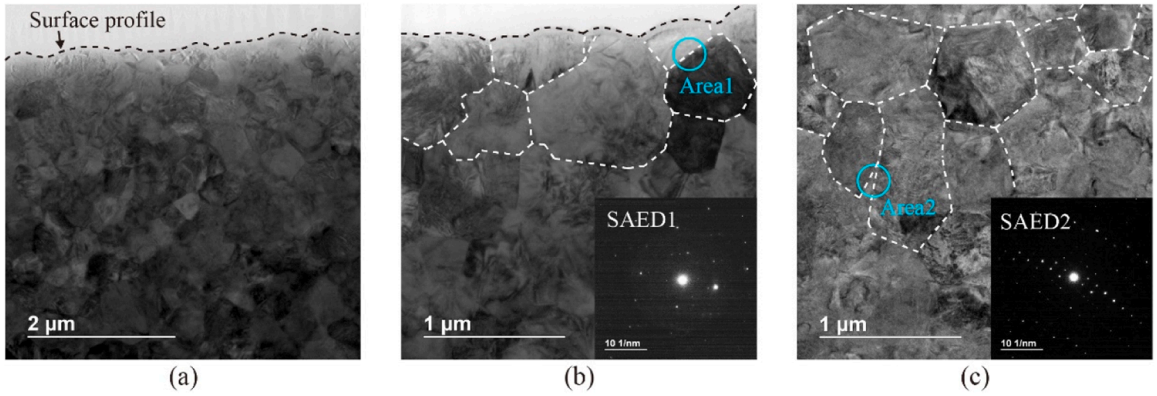

Fig. 9. Cross-sectional TEM images of the yttria-stabilized zirconia before burnishing process: (a) general view of the subsurface; (b) close-up view of the subsurface located close to the surface; (c) close-up view of the subsurface located far from the surface. The white dashed lines indicate the grain boundaries. Insets in (b) and (c) are the selected area electron diffraction (SAED) patterns of the circled areas.

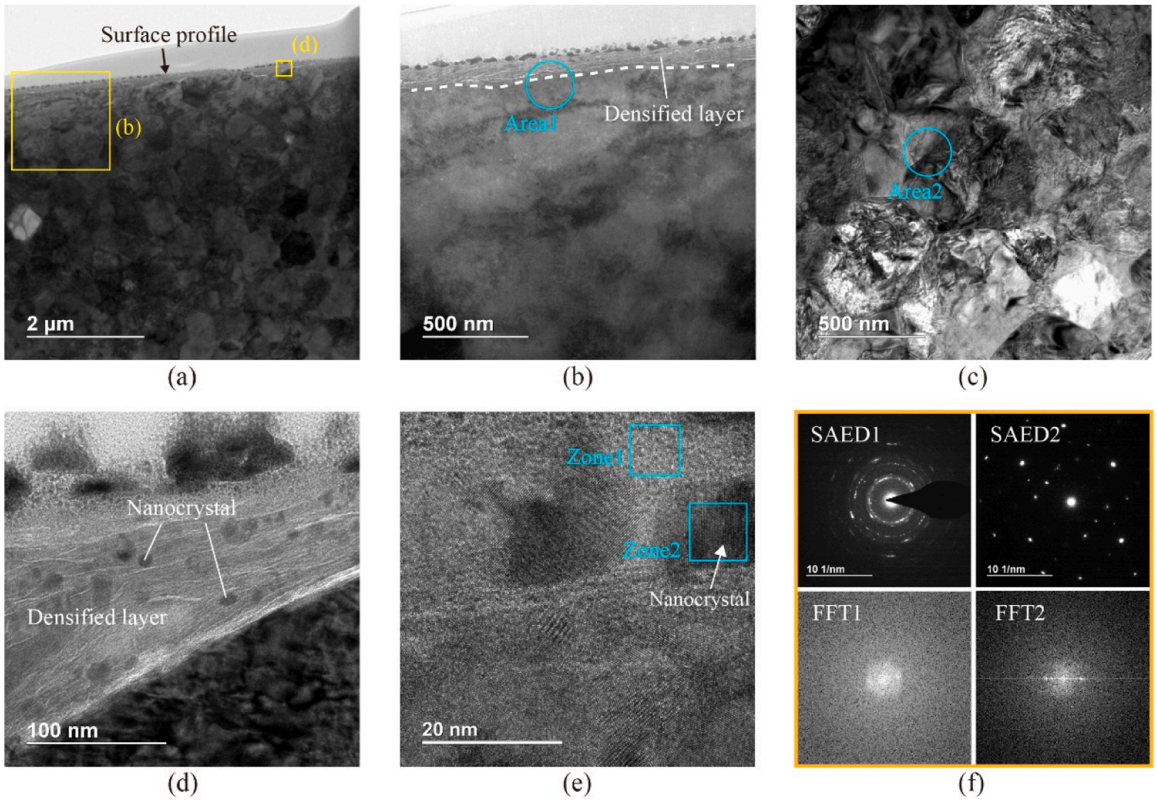

Fig. 10. Cross-sectional TEM images of the yttria-stabilized zirconia processed by ultrasonic vibration-assisted burnishing: (a) general view of the subsurface; (b) close-up view of the subsurface located close to the surface; (c) close-up view of the subsurface located far from the surface. (d) High-magnification view of the near-surface region indicated in (a). (e) High-magnification view of the densified layer. (f) Selected area electron diffraction (SAED) patterns of the circled areas indicated in (b) and (c), and Fast Fourier transform (FFT) patterns within the boxed areas indicated in (e). The burnishing test was performed under a force of 100 N, a speed of 3 mm/s, and for 1 cycle.

that the chemical composition in the densified zone is similar to other areas. These results indicate that both UVB and CB contributed to grain refinement in the near-surface layer without causing any chemical reaction.

3.5. Tool surface observation

Fig. 12a shows a SEM image of the tool surface after UVB. A bright area was observed in the center of the tool tip. According to EDX analysis, as shown in Fig. 12d, a large amount of Zr and O elements were detected in the center of the tool tip, and C element filled the outer area. As the tool is made of polycrystalline diamond, this suggests that material removal occurred during burnishing and subsequently adhered to the center of the tool tip. This is consistent with the shaved-off phenomenon observed on the workpiece surface (see Fig. 4b). Additionally, the shape of the chip adhesion area is approximately circular, which implies that the workpiece material primarily underwent compression and elastic recovery as it was scratched by the tool, forming a circular tool-work contact area. Material removal did not occur in front of the tool, as in cutting, but instead took place across the entire tool-work contact area due to the rough surface of the tool.

Fig. 12b presents a magnified image of the tool surface outside the

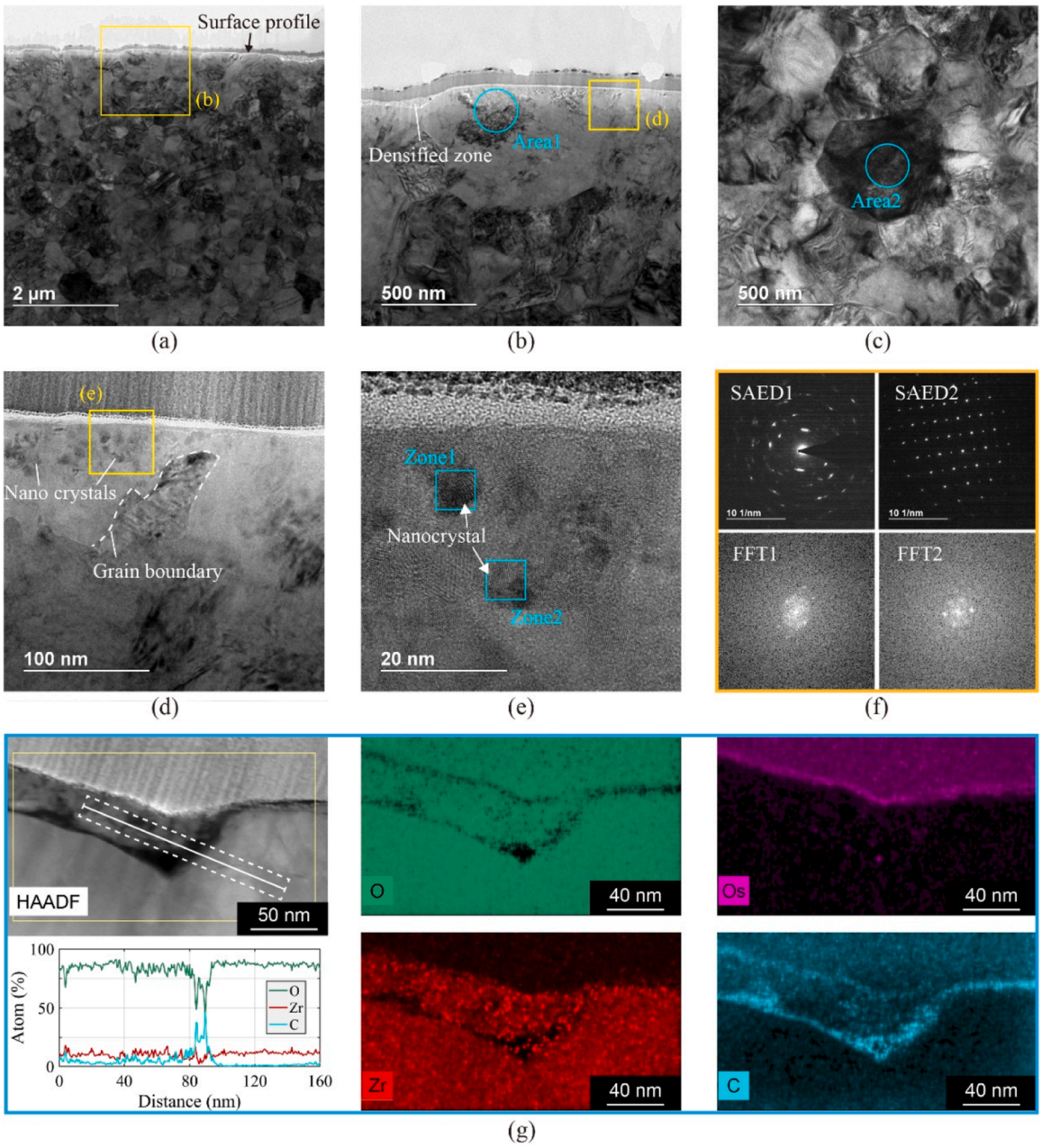

Fig. 11. Cross-sectional TEM images of the yttria-stabilized zirconia processed by conventional burnishing: (a) general view of the subsurface; (b) close-up view of the subsurface located close to the surface; (c) close-up view of the subsurface located far from the surface. (d) High-magnification view of the near-surface region indicated in (b). (e) High-magnification view of the area indicated in (d). (f) Selected area electron diffraction (SAED) patterns of the circled areas indicated in (b) and (c), and Fast Fourier transform (FFT) patterns within the boxed areas indicated in (e). (g) High-angle annular dark field (HAADF) image of an area containing a densified zone, along with the elemental mapping within the yellow rectangular box. The atomic percentage of elements was plotted along the white line based on the average within the area marked by the white dashed box. The burnishing test was performed under a force of 100 N, a speed of 3 mm/s, and for 1 cycle.

tool-work contact area, corresponding to the areas rich in carbon elements as indicated in the EDX analysis. A rough surface adhered with small particle-like chips was observed. In contrast, Fig. 12c shows a magnified view of the tool surface within the tool-work contact area. It was found that the chips adhering to the tool surface transformed into a powder-like layer due to the strong compression. Besides, within the tool-work contact area, some craters on the tool surface were not covered by chips, suggesting that these areas experience inadequate contact with the workpiece as a result of the rough tool surface. The chips adhered to the tool surface are supposed to have little impact on the integrity of the burnished surface. This is because, on one hand, they are powder with much lower hardness than the bulk material. On the other hand, the chips adhered to the tool are constantly wiped off during the machining process, while new chips continuously attach to the tool surface.

3.6. Surface hardness test

The hardness of the burnished surfaces was evaluated using nanoindentation tests at maximum loads (P_{max}) of 50 mN and 1000 mN. Typical load-displacement curves under various conditions were plotted in Fig. 13. Under the P_{max} of 1000 mN, the curves of the UVB- and CB-processed surfaces exhibit a similar trend, reaching a maximum penetration depth of approximately 1800 nm during the loading to P_{max}.

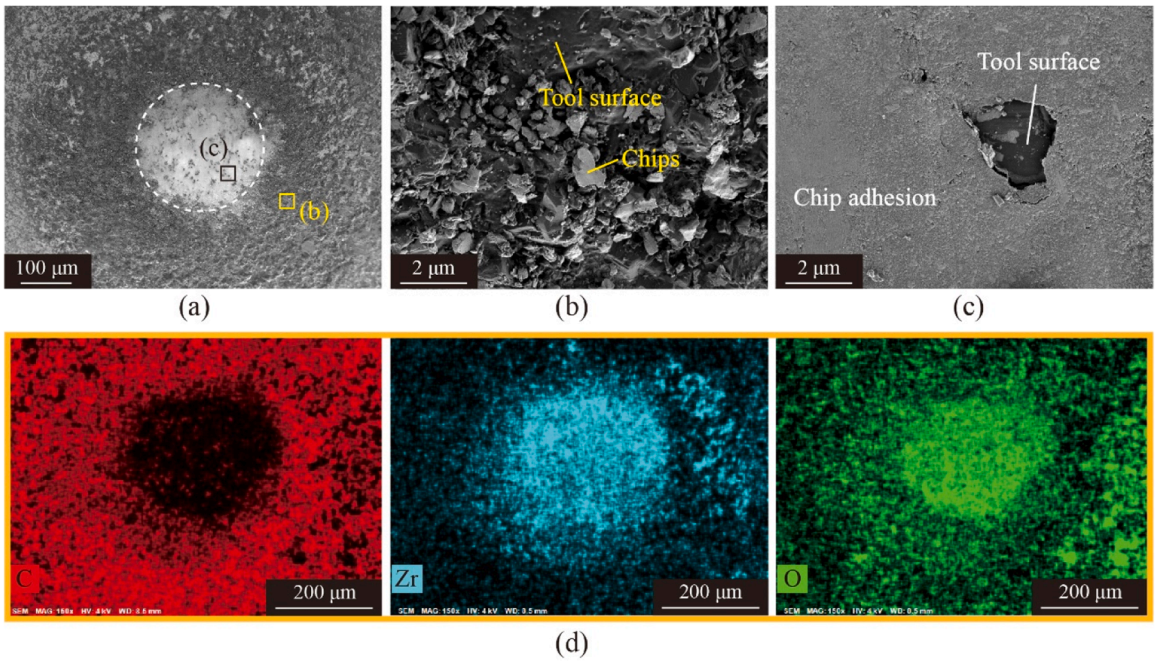

Fig. 12. SEM images of the tool surface after ultrasonic vibration-assisted burnishing: (a) overall view of the tool surface. The chip adhesion mainly occurred within the white dashed circle. (b) close-up view of the original tool surface indicated in (a); (c) close-up view of the chip adhesion indicated in (a). (d) Elemental mapping of the same area shown in (a). The burnishing test was performed under a force of 100 N, speed of 3 mm/s, and for 1 cycle.

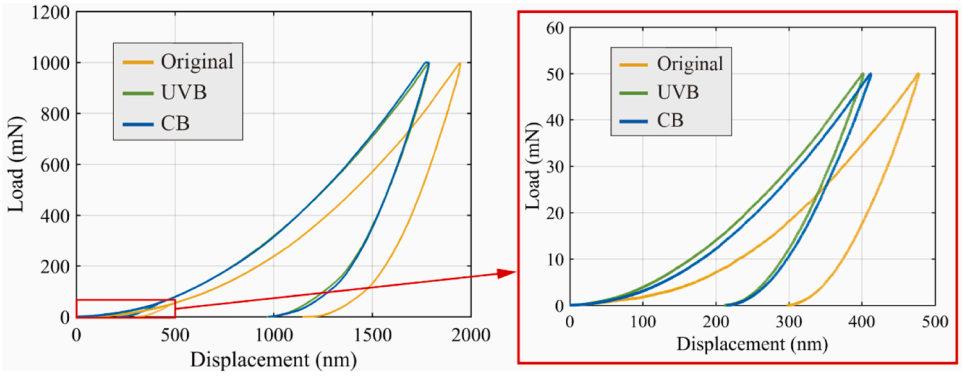

Fig. 13. Typical load-displacement curves obtained in nanoindentation tests on the original surface and the surfaces processed by ultrasonic vibration-assisted burnishing (UVB) and conventional burnishing (CB) under a force of 100 N, at a speed of 3 mm/s, and for 1 cycle.

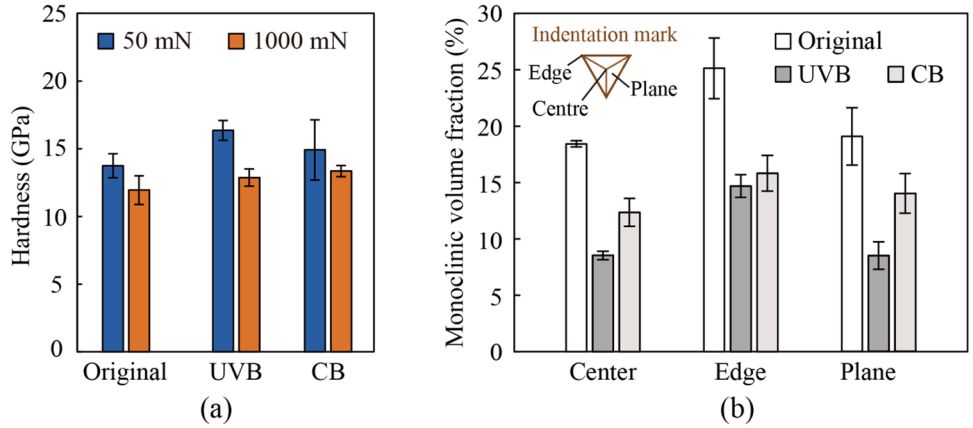

Fig. 14. Comparison of changes in (a) hardness, and (b) monoclinic volume fractions of the residual indents. The ultrasonic vibration-assisted burnishing (UVB) and conventional burnishing (CB) tests were performed under a force of 100 N, speed of 3 mm/s, and for 1 cycle. The error bars represent the standard deviations from the mean values.

Elastic recovery occurs during unloading, ultimately leaving a residual depth of approximately 980 nm. In contrast, the curve of the original surface shows a much larger penetration depth at P_{max} and a larger residual depth, which are approximately 1950 nm and 1150 nm, respectively. Under the P_{max} of 50 mN, the curves for each surface during the loading period are consistent with those at the P_{max} of 1000 mN, respectively. Zooming in on those curves, it can be seen that the curve of the original surface produces a much greater depth than the curves of the burnished surfaces at the beginning of the loading period, indicating surface hardening by the burnishing process. The curve of the UVB-processed surface always has a smaller penetration depth compared with that of the CB-processed surface under the same load, indicating more intensive hardening near the surface by UVB. The hardness value of each surface was calculated based on the load-displacement curves, and compared with one another, as shown in Fig. 14a. Under an indentation load of 50 mN, the original surface hardness was approximately 13.7 GPa, while the CB-processed surface hardness increased to approximately 14.9 GPa, and the UVB-processed surface hardness reached an even higher value of approximately 16.4 GPa. In other words, the hardness of the surface processed with UVB increased by 10 % compared to that processed with CB, and by 19.7 % compared to the original surface hardness. When the indentation load was 1000 mN, the original surface hardness reduced to approximately 11.9 GPa due to the indentation size effect. Both UVB- and CB-processed surfaces showed a hardness approximately 10 % higher than the original surface, but the hardness difference between UVB- and CB-processed surfaces was not significant. This suggests that the enhancement of surface hardening by UVB is concentrated only near the surface at shallow depths compared to CB, which is consistent with the observations in the subsurface cross-section.

To detect possible phase changes on burnished surfaces caused by external mechanical impacts, Raman spectra of the edges, centres, and planes of the residual indents produced by the nanoindentation test were examined, and their monoclinic volume fractions were calculated. The results are shown in Fig. 14b. Although the indentation deformation significantly increased V_m compared to the state before the indentation (see Fig. 8a), indicating that the indentation caused t-m phase transformation, the extent of the transformation on the CB-processed surface was smaller than that on the original surface. Moreover, after indentation on the three types of surfaces, the UVB-processed surface exhibited the lowest t-m phase transformation.

4. Discussions

4.1. Surface morphology formation mechanism

Unlike metal burnishing, which plastically deforms the workpiece surface without material removal, the burnishing of YSZ involves a small amount of material removal, evidenced by SEM images showing grains being shaved off (see Fig. 4b) and the tool adhering to fine, powder-like chips after the burnishing (see Fig. 12c). This is due to the relatively hard and brittle nature of YSZ compared to workpiece materials such as various alloys [20,21] and stainless steel [22], as well as the rougher surface of the applied polycrystalline diamond tool in contrast to single-crystal diamond tools [25]. Although material removal occurs during the burnishing of YSZ, it also differs from cutting or grinding processes where large amounts of material are removed, resulting in machined surfaces closely replicating the tool path in the depth direction. This distinction is evident from Fig. 5c, which shows that in the burnishing direction, only sharp features of the burnished surface were smoothed while the overall waviness remained unchanged. Additionally, significant elastic recovery of the workpiece material occurred during the burnishing, resulting in a rounded tool-workpiece contact area with chip adhesions present within it (see Fig. 12a).

Therefore, based on the above analysis, a model of burnishing-to-cutting was proposed to explain the formation mechanisms of surface morphology during the burnishing of YSZ, as illustrated in Fig. 15. From a macroscopic perspective (see Fig. 15a), due to the extremely large tool radius and small burnishing depth, the workpiece material in front of the tool flows completely downward and undergoes compression. Given the limited plasticity of YSZ, the compressed material mostly undergoes elastic recovery after the tool passes. From a microscopic perspective, the rough tool surface slides over the rough workpiece surface. The submicron-scale protrusions on the tool surface act as cutting edges, penetrating the workpiece material and partially removing workpiece in areas where there is local interference between the tool and the workpiece as the tool moves forward. This process will occur in all areas of contact between the tool and the workpiece, as depicted in Fig. 15b,c. This is similar to the abrasive wear process that takes place when a hard rough surface slides across a softer surface [37]. However, the front part of the tool (see Fig. 15b) initially tends to remove the sharp features from the workpiece surface to achieve a relatively smooth surface, while the rear part of the tool (see Fig. 15c) tends to scratch the surface already machined by the front part of the tool, resulting in a smoother workpiece surface. Furthermore, during the UVB process, the burnishing depth is estimated to be approximately 6 μm based on the tool radius (see Fig. 2a) and the width of the burnished area (see Fig. 5a). Given that the tool vibration amplitude is approximately 2 μm, although the central area of the tool is expected to be in continuous contact with the workpiece like in CB process, the outer areas of the tool intermittently contact the workpiece due to the tool vibration. As a result, the front and rear parts of the tool intermittently engage with the workpiece, promoting interface lubrication and reducing burr formation. Although certain irregular submicron-scale protrusions on the tool may impact the workpiece material as the tool vibrates, causing numerous periodic marks to be imprinted along the burnishing direction, the overall surface quality produced by UVB is better than that produced by CB.

4.2. Subsurface structural evolution mechanism

The tetragonal phase of YSZ tends to transform into the monoclinic phase under high tensile and shear stress conditions involving unconstrained volume expansion [38] or under uniaxial tensile and compressive loads, while hydrostatic tensile and compressive loadings do not [39]. The cyclic indentation of YSZ revealed that the extent of the t-m phase transformation varies at different locations within the residual indents [27]. The region beneath the indent plane, dominated by shear stress, exhibited the highest V_m, whereas the region beneath the indent centre, dominated by hydrostatic compressive stress, showed the lowest V_m. In contrast, during the burnishing process, the burnishing tool makes contact with the workpiece over a large area. This contact geometry enhanced the hydrostatic compressive stress and constrained the volume change of the material. Hence, the structural changes induced by burnishing differ significantly from those caused by cutting and indentation, where a sharp tool/indenter is used. In the latter, the shear stress produced by the sharp edge/tip dominates the material removal and deformation. Consequently, the monoclinic volume fraction of the burnished surface decreased, whereas that of the cut surface increased [12].

A combination of high compressive and shear stresses in burnishing process causes intensive dislocation initiation/growth in the material, resulting in grain refinement in the near-surface region, as shown in the schematic model in Fig. 16a. The residual compressive stress in the grain-refined layer after burnishing further increased surface hardness and additionally inhibited monoclinic phase formation by restricting volume expansion [40]. Furthermore, in UVB, the ultrasonic vibration induces a hammering effect that periodically impacts the refined layer, causing material densification, which further enhances the compressive stress and surface hardening, as shown in Fig. 16b. This is a hybrid effect of burnishing and ultrasonic impact, which generates a hardened layer on the workpiece surface with a strong resistance to external loads and mechanical damage Therefore, the UVB process could provide

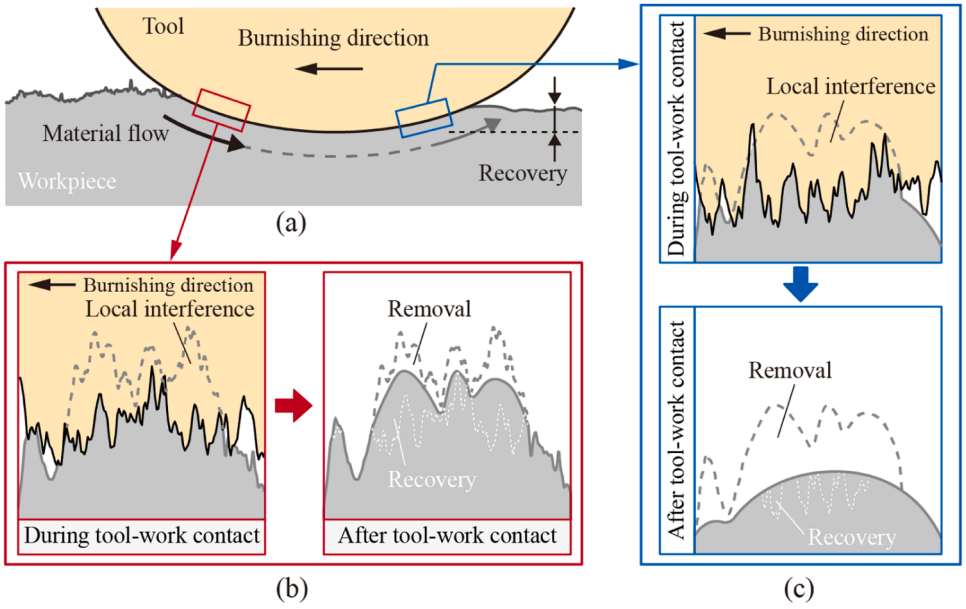

Fig. 15. Schematic of the formation mechanism of surface morphology in burnishing process: (a) Macroscopic burnishing. (b) Microscopic multi-point cutting at the front part of the tool. (c) Microscopic multi-point cutting at the rear part of the tool. In (b) and (c), the black solid lines are the tool surface profiles. The grey dashed lines are the workpiece surface profiles before the tool contacting. The grey solid lines are the workpiece surface profiles not in contact with the tool. The white dashed lines are the workpiece surface profiles during the tool contacting, which align with the black solid tool surface profiles. Therefore, during the tool-work contact, the areas of interference between the tool and the workpiece, which lie between the grey dashed line and the black solid line, tend to be removed by the tool. After tool-work contact, the areas in the workpiece that interferes with the tool are partially removed, while the remaining areas exhibit elastic recovery.

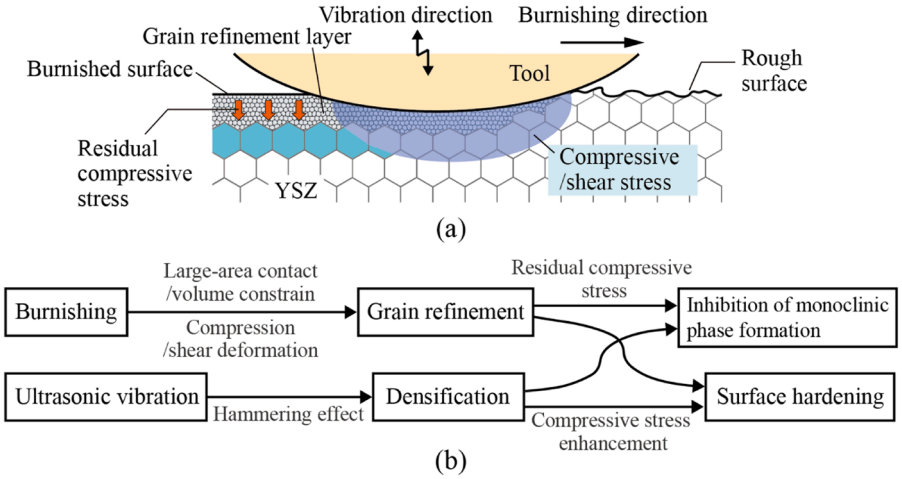

Fig. 16. Mechanisms of subsurface microstructural evolution in ultrasonic vibration-assisted burnishing: (a) schematic model showing the grain refinement of yttria-stabilized zirconia (YSZ) under compressive/shear stresses applied by a blunt tool; and (b) flowchart of the effects of burnishing and ultrasonic vibration factors on the subsurface microstructural evolution.

advantages in strengthening the subsurface of YSZ in terms of phase transformation and hardness compared to diamond turning [27] or abrasive machining [41], although it cannot achieve as good surface roughness as the latter processes. Sandblasting, etching, and laser treatment have been used for the surface modification of YSZ [42]. These methods effectively modify surface topography but do not induce significant compressive stress. Therefore, burnishing is superior to these methods for modifying the subsurface microstructures, which may be helpful in those YSZ parts used in heavy-duty applications. Additionally, since burnishing mainly relies on compression deformation rather than material removal, it produces little waste. It is an economical and environmentally sustainable technique for modifying YSZ parts.

Moreover, it is important to note that the ageing of YSZ, a spontaneous time-dependent degradation related to the t-m phase transformation, inevitably occurs, especially when exposed to water or water vapor. As ageing progresses through the ceramic surface and subsurface, it may promote the formation of microcracks in areas neighbouring the grains and even cause grain detachment/pullout, thereby increasing surface roughness, which negatively impacts the strength and fracture toughness of fabricated YSZ parts [43]. Since it has been found that a compressive residual stress layer in the top surface of the workpiece is beneficial for ageing resistance [44], processing the YSZ surface with UVB may decrease its susceptibility to ageing.

5. Conclusions

Ultrasonic vibration-assisted burnishing (UVB) was performed on yttria stabilized zirconia (YSZ) under various conditions and compared

with those results obtained through conventional burnishing (CB). Mechanisms of surface morphology formation and subsurface microstructure evolution during burnishing were revealed by characterizing both the surface morphology and subsurface microstructure of the workpiece, as well as tool conditions. Nanoindentation tests were performed on burnished surfaces to verify hardening effect on YSZ. The resulting subsurface damages were also characterized. The following conclusions can be drawn:

(1) Surface roughness decreased with more burnishing cycles and higher burnishing force, while it was less affected by the burnishing speed. However, if the burnishing force exceeded a critical value, the surface quality began to deteriorate due to the ploughing effect caused by the increased burnishing depth. After 30 cycles of burnishing at a force of 100 N, the surface achieved a smoothness of 0.12 μm Ra, resulting in a 67.6 % reduction in roughness compared to the original sintered surface.
(2) Macroscopic burnishing and microscopic multi-point cutting collectively contribute to surface smoothing in the burnishing of YSZ, resulting in a finish that is not only far better than the tool's surface roughness but also significantly smoother than the original workpiece's surface roughness. The microscopic cutting involves material removal by shaving off with the rough surface of the tool.
(3) The burnishing-induced compressive stress and material densification could suppress the formation of the monoclinic phase during the processing of YSZ. UVB produced a hammering effect that further enhanced subsurface residual stress and grain refinement area, and led to a continues densification zone within the top of the grain refinement layer.
(4) Significant surface hardening occurred after UVB due to the grain refinement. The grain refinement layer resulted in an increased surface hardness of up to 19.7 % compared to the original surface when subjected to a maximum 50 mN indentation load.
(5) The UVB-processed surface demonstrated strong resistance to subsequent indentation damage, exhibiting minimal tetragonal-to-monoclinic phase transformation in the residual indents compared to the original and CB-processed surfaces.

The results of this study demonstrated new possibilities for improving the surface quality and subsurface property of YSZ in one step by UVB, which is expected to contribute to the future manufacturing of YSZ products with enhanced surface functionality. Nevertheless, due to its hard and brittle properties, the current burnishing techniques for metals cannot efficiently process YSZ. Further work on controlling processing conditions to reduce variability in surface integrity is needed. Additionally, a statistical investigation of burnishing characteristics of YSZ is required.

CRediT authorship contribution statement

Weihai Huang: Writing – original draft, Visualization, Validation, Methodology, Investigation, Data curation, Formal analysis. **Toshiki Tsuchida**: Writing – original draft, Methodology, Investigation, Data curation, Formal analysis. **Jiwang Yan**: Writing – review & editing, Conceptualization, Methodology, Investigation, Supervision, Resources, Project administration, Funding acquisition.

Declaration of Competing Interest

The authors declare that they have no known competing financial interests or personal relationships that could have appeared to influence the work reported in this paper.

Acknowledgements

This work has been partially supported by Japan Society for the Promotion of Science, Grant-in-Aid for Scientific Research (B), project number 21H01230. The authors would like to thank TOSOH Corporation for providing the experimental samples.

References

[1] Roitero, E., Reveron, H., Gremillard, L., Garnier, V., Ritzberger, C., Chevalier, J., 2023. Ultra-fine Yttria-Stabilized Zirconia for dental applications: a step forward in the quest towards strong, translucent and aging resistant dental restorations. J. Eur. Ceram. Soc. 43, 2852–2863.
[2] Piconi, C., Condo, S.G., Kosmač, T., 2014. Chapter 11 - Alumina- and Zirconia-based Ceramics for Load-bearing Applications. Advanced Ceramics for Dentistry 219–253. https://doi.org/10.1016/B978-0-12-394619-5.00011-0.
[3] Cho, J., Li, J., Li, Q., Ding, J., Wang, H., Xue, S., Holland, T.B., Mukherjee, A.K., Wang, H., Zhang, X., 2018. In-situ high temperature micromechanical testing of ultrafine grained yttria-stabilized zirconia processed by spark plasma sintering. Acta Mater. 155, 128–137.
[4] Yamamuro, Y., Shimoyama, T., Nagata, H., Yan, J., 2024. Effect of dopant concentration on femtosecond pulsed laser irradiation of yttria-stabilized zirconia for generating nanopores. J. Alloy. Compd. 980, 173596.
[5] Garvie, R.C., Hannink, R.H., Pascoe, R.T., 1975. Ceramic steel? Nature 258, 703–704.
[6] Ming, Y., Huang, X., Zhou, D., Li, X., 2022. A novel Non-Newtonian fluid polishing technique for zirconia ceramics based on the weak magnetorheological strengthening thickening effect. Ceram. Int. 48, 7192–7203.
[7] Krishnamurthy, R., Arunachalam, L.M., Gokularathnam, C.V., Venkatesh, V.C., 1991. Grinding of Transformation-Toughened Y-TZP Ceramics. CIRP Ann. 40, 331–333.
[8] Yoon, H., Lee, S., Min, S., 2018. Investigation of ductile-brittle transition in machining of yttrium-stabilized zirconia (YSZ). Procedia Manuf. 26, 446–453.
[9] Ma, Z., Wang, Q., Chen, H., Chen, L., Qu, S., Wang, Z., Yu, T., 2022. A grinding force predictive model and experimental validation for the laser-assisted grinding (LAG) process of zirconia ceramic. J. Mater. Process. Technol. 302, 117492.
[10] Kizaki, T., Ogasahara, T., Sugita, N., Mitsuishi, M., 2014. Ultraviolet-laser-assisted precision cutting of yttria-stabilized tetragonal zirconia polycrystal. J. Mater. Process. Technol. 214, 267–275.
[11] Kizaki, T., Harada, K., Mitsuishi, M., 2014. Efficient and precise cutting of zirconia ceramics using heated cutting tool. CIRP Ann. 63, 105–108.
[12] Yan, J., Okuuchi, T., 2019. Chip morphology and surface integrity in ultraprecision cutting of yttria-stabilized tetragonal zirconia polycrystal. CIRP Ann. 68, 53–56.
[13] Lan, T., Wang, C., Chen, K., Wang, M., Lee, H., 2017. Milling properties of low temperature sintered zirconia blocks for dental use. Mater. Sci. Eng. C 73, 692–699.
[14] De Souza, R.H., Kaizer, M.R., Borges, C.E.P., Fernandes, A.B.F., Correr, G.M., Diógenes, A.N., Zhang, Y., Gonzaga, C.C., 2020. Flexural strength and crystalline stability of a monolithic translucent zirconia subjected to grinding, polishing and thermal challenges. Ceram. Int. 46, 26168–26175.
[15] Wan, L., Li, L., Deng, Z., Deng, Z., Liu, W., 2019. Thermal-mechanical coupling simulation and experimental research on the grinding of zirconia ceramics. J. Manuf. Process. 47, 41–51.
[16] Li, F.L., Xia, W., Zhou, Z.Y., Zhao, J., Tang, Z.Q., 2012. Analytical prediction and experimental verification of surface roughness during the burnishing process. Int. J. Mach. Tools Manuf. 62, 67–75.
[17] Huang, W., Yan, J., 2023. Effect of tool geometry on ultraprecision machining of soft-brittle materials: a comprehensive review. Int. J. Extrem. Manuf. 5, 012003.
[18] Balland, P., Tabourot, L., Degre, F., Moreau, V., 2013. An investigation of the mechanics of roller burnishing through finite element simulation and experiments. Int. J. Mach. Tools Manuf. 65, 29–36.
[19] Ma, C., Andani, M.T., Qin, H., Moghaddam, N.S., Ibrahim, H., Jahadakbar, A., Amerinatanzi, A., Ren, Z., Zhang, H., Doll, G.L., Dong, Y., Elahinia, M., Ye, C., 2017. Improving surface finish and wear resistance of additive manufactured nickel-titanium by ultrasonic nano-crystal surface modification. J. Mater. Process. Technol. 249, 433–440.
[20] Yang, S., Umbrello, D., Dillon, O.W., Puleo, D.A., Jawahir, I.S., 2015. Cryogenic cooling effect on surface and subsurface microstructural modifications in burnishing of Co–Cr–Mo biomaterial. J. Mater. Process. Technol. 217, 211–221.
[21] Revankar, G.D., Shetty, R., Rao, S.S., Gaitonde, V.N., 2017. Wear resistance enhancement of titanium alloy (Ti–6Al–4V) by ball burnishing process. J. Mater. Res. Technol. 6, 13–32.
[22] Konefal, K., Korzynski, M., Byczkowska, Z., Korzynska, K., 2013. Improved corrosion resistance of stainless steel X6CrNiMoTi17-12-2 by slide diamond burnishing. J. Mater. Process. Technol. 213, 1997–2004.
[23] Zhang, K., Liu, S., Wang, J., Sun, Z., Liu, W., Zhang, C., Zhang, X., 2024. Effect of high-frequency dynamic characteristics in the ultrasonic surface rolling process on the surface properties. J. Mater. Process. Technol. 327, 118353.
[24] Jerez-Mesa, R., Travieso-Rodriguez, J.A., Gomez-Gras, G., Lluma-Fuentes, J., 2018. Development, characterization and test of an ultrasonic vibration-assisted ball burnishing tool. J. Mater. Process. Technol. 257, 203–212.
[25] Huang, W., Yan, J., 2021. Chip-free surface patterning of toxic brittle polycrystalline materials through micro/nanoscale burnishing. Int. J. Mach. Tools Manuf. 162, 103688.

[26] Tsuchida, T., Huang, W., Yan, J., 2024. Surface conditioning of zirconia ceramic by enhanced ultrasonic vibration-assisted burnishing. Prod. Eng. 18, 353–366.
[27] Kosai, K., Yan, J., 2020. Effects of cyclic loading on subsurface microstructural changes of zirconia polycrystals in nanoscale mechanical processing. Int. J. Mach. Tools Manuf. 159, 103626.
[28] Yang, H., Xie, J., He, Q., Liu, J., Shi, Y., 2023. Study on diamond cutting-to-burnishing for thermal-force dispersion in dry metal grinding. J. Mater. Process. Technol. 313, 117874.
[29] Zhou, Z., Zheng, Q., Ding, C., Yan, J., Piao, Z., 2021. Effect of surface burnishing process with different strain paths on the copper microstructure. J. Manuf. Process. 71, 653–668.
[30] Korzynski, M., 2007. Modeling and experimental validation of the force–surface roughness relation for smoothing burnishing with a spherical tool. Int. J. Mach. Tools Manuf. 47, 1956–1964.
[31] Rahman, M.A., Amrun, M.R., Rahman, M., Kumar, A.S., 2017. Variation of surface generation mechanisms in ultra-precision machining due to relative tool sharpness (RTS) and material properties. Int. J. Mach. Tools Manuf. 115, 15–28.
[32] Zhou, Z., Zheng, Q., Ding, C., Yan, J., Peng, G., Piao, Z., 2021. Research on the promotion mechanism of surface burnishing process by two-dimensional ultrasonic vibration. J. Mater. Res. Technol. 13, 1068–1082.
[33] Quirk, J., Rothmann, M., Li, W., Abou-Ras, D., McKenna, K.P., 2024. Grain boundaries in polycrystalline materials for energy applications: First principles modeling and electron microscopy. Appl. Phys. Rev. 11, 011308.
[34] Choudhary, A., Paul, S., 2021. Surface generation in high-speed grinding of brittle and tough ceramics. Ceram. Int. 47, 30546–30562.
[35] Edalati, K., Toh, S., Ikoma, Y., Horita, Z., 2011. Plastic deformation and allotropic phase transformations in zirconia ceramics during high-pressure torsion. Scr. Mater. 65, 974–977.
[36] Muñoz Tabares, J.A., Anglada, M.J., 2010. Quantitative Analysis of Monoclinic Phase in 3Y-TZP by Raman Spectroscopy. J. Am. Ceram. Soc. 93, 1790–1795.
[37] Monaca, A.L., Murray, J.W., Liao, Z., Speidel, A., Robles-Linares, J.A., Axinte, D.A., Hardy, M.C., Clare, A.T., 2021. Surface integrity in metal machining - Part II: Functional performance. Int. J. Mach. Tools Manuf. 164, 103718.
[38] Chintapalli, R.K., Jimenez-Pique, E., Marro, F.G., Yan, H., Reece, M., Anglada, M., 2012. Spherical instrumented indentation of porous nanocrystalline zirconia. J. Eur. Ceram. Soc. 32, 123–132.
[39] Deng, B., Luo, J., Harris, J.T., Smith, C.M., 2020. Critical stress map for ZrO2 tetragonal to monoclinic phase transformation in ZrO2-toughened glass-ceramics. Materialia 9, 100548.
[40] Muñoz-Tabares, J.A., Jiménez-Piqué, E., Reyes-Gasga, J., Anglada, M., 2012. Microstructural changes in 3Y-TZP induced by scratching and indentation. J. Eur. Ceram. Soc. 32, 3919–3927.
[41] Minguela, J., Ginebra, M.P., Llanes, L., Mas-Moruno, C., Roa, J.J., 2020. Influence of grinding/polishing on the mechanical, phase stability and cell adhesion properties of yttria-stabilized zirconia. J. Eur. Ceram. Soc. 40, 4304–4314.
[42] Soon, G., Pingguan-Murphy, B., Lai, K.W., Akbar, S.A., 2016. Review of zirconia-based bioceramic: surface modification and cellular response. Ceram. Int. 42, 12543–12555.
[43] Chevalier, J., 2006. What future for zirconia as a biomaterial? Biomaterials 27, 535–543.
[44] Deville, S., Chevalier, J., Gremillard, L., 2006. Influence of surface finish and residual stresses on the ageing sensitivity of biomedical grade zirconia. Biomaterials 27, 2186–2192.